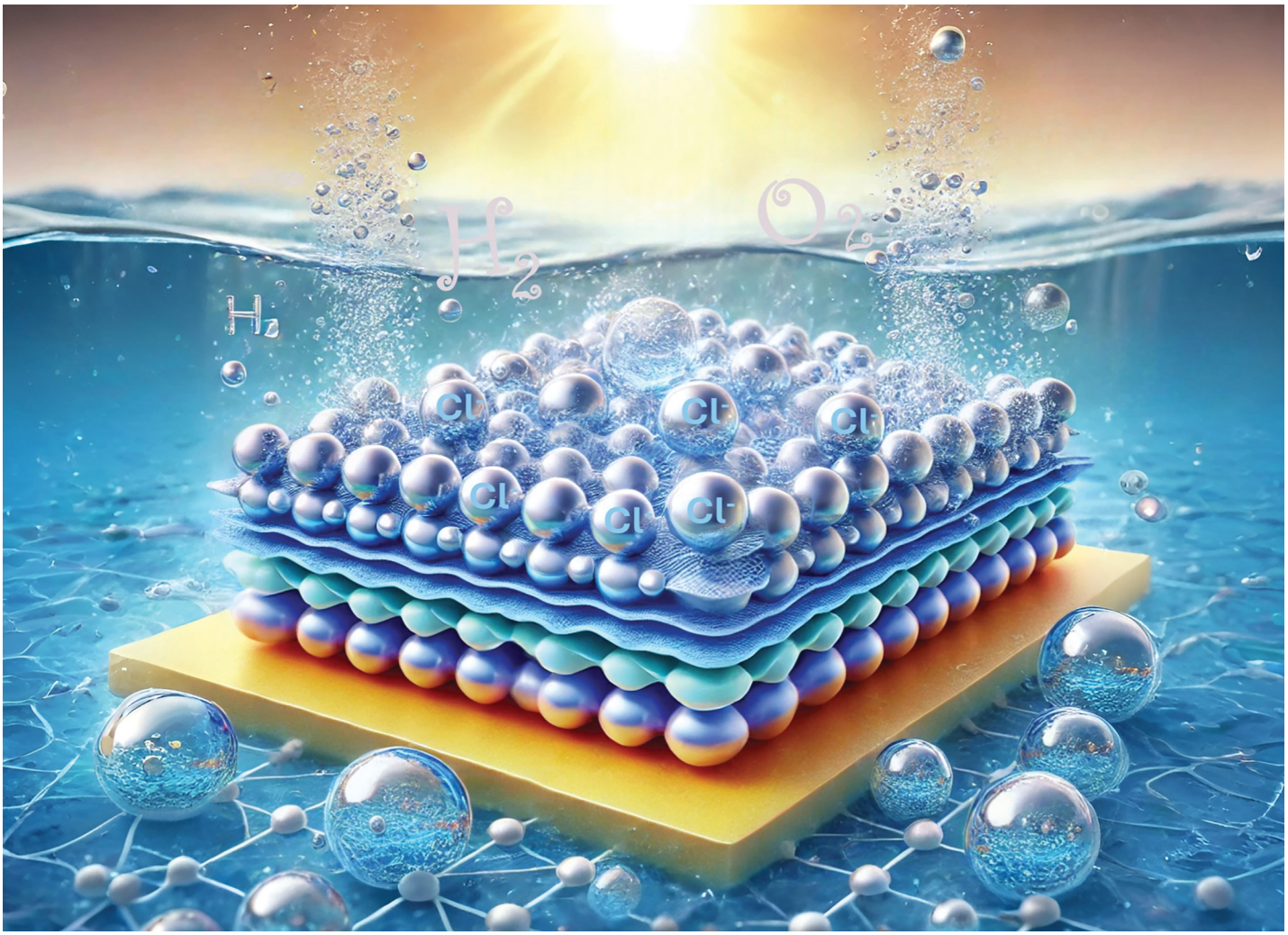

Showcasing research from Professor Song's laboratory, Department of Energy Engineering, Hanyang University, Seoul, Republic of Korea.

Tailoring the electronic structure of an exfoliated layered double hydroxide using a lanthanide for chloride-ion blocking in seawater splitting

Seawater is a widely available source of hydrogen in our environment, possessing significant potential for hydrogen generation. The chloride ion is the primary component in seawater splitting, as it can hinder the active site responsible for *OH adsorption. Consequently, it became imperative to inhibit the chloride ion from reaching the active site. We employed the concept of Lewis acidity for the inhibition of the chloride ion. The Lewis acidity of Ni^{2+} and Fe^{3+} ions is augmented by Ce doping *via* electronic manipulation.

Image reproduced by permission of HyukSu Han from *EES Catal.*, 2025, **3**, 435.

As featured in:

See Chan-Yeup Chung, HyukSu Han, Taeseup Song *et al.*, *EES Catal.*, 2025, **3**, 435.

ROYAL SOCIETY OF CHEMISTRY

rsc.li/EESCatalysis

Registered charity number: 207890

EES Catalysis

PAPER

View Article Online
View Journal | View Issue

Open Access Article. Published on 27 febbraio 2025. Downloaded on 26/12/2025 23:20:05.
This article is licensed under a Creative Commons Attribution-NonCommercial 3.0 Unported Licence.

Check for updates

Cite this: *EES Catal.*, 2025, 3, 435

Tailoring the electronic structure of an exfoliated layered double hydroxide using a lanthanide for chloride-ion blocking in seawater splitting†

Ashish Gaur,‡[a] Jiseok Kwon,‡[b] Jatin Sharma,[a] Ghulam Ali,[c] Enkhtuvshin Enkhbayar,[a] Chan-Yeup Chung,*[d] HyukSu Han*[a] and Taeseup Song*[b]

Received 13th December 2024,
Accepted 14th February 2025

DOI: 10.1039/d4ey00278d

rsc.li/eescatalysis

Seawater is one of the most abundant sources of hydrogen in our environment, and it has great potential for the production of hydrogen *via* water electrolysis. However, seawater electrolysis is challenging as chloride ions could obstruct catalytic active sites, reducing *OH adsorption. Therefore, it is crucial to prevent chloride ions from accessing the active sites. Herein, we modulated the Lewis acidity of electrocatalysts to solve this problem. In particular, the Lewis acidity of Ni^{2+} and Fe^{3+} ions in a layered double hydroxide (LDH) was enhanced by incorporating the lanthanide dopant Ce, thereby tuning the surface electronic configurations to prefer OH* adsorption over Cl* adsorption. Further, the Ce-doped Ni–Fe LDH (CNF-LDH) was exfoliated *via* the O_2 plasma process to improve the accessibility of active sites for intermediates. The resultant CNF-LDH-E exhibited an overpotential of 230 and 169 mV at 100 mA cm^{-2} for OER and HER, respectively, in alkaline freshwater (1 M KOH) and 290 and 285 mV, respectively, in simulated seawater (1 M KOH + 0.1 M NaCl) electrolytes. The impact of Lewis acidity on blocking the chloride ions was further investigated using density functional theory (DFT) calculations.

Broader context

Recently, there has been a significant increase in research focused on the production of hydrogen using the process of electrochemical seawater splitting. Nevertheless, electrode performance and durability are constrained by many obstacles that must be resolved to ensure the technological suitability of this process for industrial applications. The presence of chloride ions in saltwater obstructs the active site, resulting in chloride corrosion. This corrosion is the primary concern as it has detrimental effects on both the performance and durability of the anode component. To address this particular problem, we developed an electrode that contains Ce-incorporated NiFe-oxyhydroxides for splitting seawater. In addition, the active sites were significantly increased using the argon plasma exfoliation technique. The efficacy of the aforementioned methodologies was shown by combining theoretical calculations and experimental results. This investigation provides an excellent manual for the rational design of catalysts that are both efficient and robust for the electrolysis of seawater.

Introduction

Hydrogen is often considered the best alternative for tackling global energy challenges. Hydrogen energy possesses significant potential owing to its exceptionally high gravimetric energy density.[1,2] Currently, coal gasification or methane reforming processes are practically applied in industries to produce hydrogen. However, both processes release a significant amount of global-warming CO_2 gas along with potentially harmful byproducts.[3–6] Water splitting has a high potential to provide an environmentally benign alternative to hydrogen generation. However, current water electrolysis techniques primarily rely on freshwater, which is limited on our planet. Therefore, we must shift our attention towards utilizing seawater for commercial hydrogen generation.[7–9] On the one hand, indirect seawater electrolysis (ISE) necessitates

[a] *Department of Energy Science, Sungkyunkwan University, 2066 Seobu-ro, Jangan-gu, Suwon-si, Gyeonggi-do 16419, Republic of Korea. E-mail: hyuksuhan@skku.edu*
[b] *Department of Energy Engineering, Hanyang University, 222 Wangsimni-ro, Seongdong-gu, Seoul 04763, Republic of Korea. E-mail: tssong@hanyang.ac.kr*
[c] *U.S.-Pakistan Center for Advanced Studies in Energy (USPCASE), National University of Sciences and Technology (NUST), H-12, Islamabad, Pakistan*
[d] *Bass Co. LTD., 1121 Beoman-ro, Geumcheon-gu, Seoul, 08594, Republic of Korea. E-mail: chanyeup.chung@gmail.com*

† Electronic supplementary information (ESI) available. See DOI: https://doi.org/10.1039/d4ey00278d

‡ Both the authors contributed equally.

© 2025 The Author(s). Published by the Royal Society of Chemistry

Open Access Article. Published on 27 febbraio 2025. Downloaded on 26/12/2025 23:20:05.
This article is licensed under a Creative Commons Attribution-NonCommercial 3.0 Unported Licence.

the implementation of a sophisticated water desalination system before electrolysis, increasing the complexity of the system and diminishing its long-term viability for industrial hydrogen generation.[10–12] On the other hand, the direct seawater electrolysis (DSE) method, which eliminates the need for supplementary pre-electrolysis systems, can substantially lower the production costs of green hydrogen.[13–18] Thus, DSE is an attractive technique towards practical hydrogen production from seawater, but several challenges need to be overcome for its realization.

The average quantity of salt in seawater is approximately 3.5 wt%, where the chloride ion has the largest concentration among all the ions present in the seawater.[19–21] Thus, chloride and water oxidation reactions compete at the anode.[22–24] According to the Pourbaix diagram, the oxygen evolution reaction (OER) becomes more favourable than the chlorine evolution reaction (CER) as the pH of the electrolyte increases, implying the advantages of alkaline seawater splitting.[25–30] Hence, the anode must possess high selectivity for the adsorption of hydroxyl ions while blocking chloride ions to successfully split alkalized seawater.[31–33] Guo *et al.* introduced a hard Lewis acid layer (Cr_2O_3) over the surface of the catalyst (CoO_x) to repel Cl^- ions and simultaneously capture OH^- ions.[34] Owing to the high oxidation number of Cr^{3+} in Cr_2O_3, it is considered a hard Lewis acid that can selectively capture a hard Lewis base OH^-. This signifies that metals with a higher oxidation state can selectively capture OH^-, inhibiting chloride corrosion during seawater splitting.

Layered double hydroxide (LDH) materials have been extensively studied for freshwater electrolysis, but their potential for seawater electrolysis remains undefined.[35–38] In this work, we intended to improve the electrocatalytic activity of the nickel–iron LDH by introducing a lanthanide dopant of Ce (CNF-LDH) for seawater electrolysis. The addition of Ce to the Ni–Fe LDH led to an increase in the valence states of Ni and Fe, increasing their Lewis acidity and thus making them more favourable for capturing OH^- ions while also blocking Cl^- ions simultaneously. Further, the number of active sites of the CNF-LDH was greatly enhanced by exfoliating the stacked layers in a two-dimensional LDH structure using the O_2 plasma treatment (CNF-LDH-E).

This resulted in a substantially reduced overpotential for OER, shifting the working potential for seawater splitting to avoid the potential at which CER occurs. In addition, the morphological study confirmed the exfoliation of the stacked sheets, while the XAS and XPS studies revealed the formation of high-valent transition metal species on the CNF-LDH-E surface. Further, density functional theory (DFT) calculations indicated the unfavourable ΔG_{Cl^*} on the CNF-LDH-E, supporting our hypothesis. The final catalyst demonstrated exceptional bifunctional activity in both alkaline freshwater and seawater. The obtained overpotential for the alkaline freshwater is 230 mV (290 mV in alkalized seawater) and 169 mV (285 mV in alkalized seawater) at 100 mA cm^{-2} for the OER and hydrogen evolution reaction (HER), respectively. We believe that this work opens up novel possibilities for the creation of chloride ion-blocking materials in the field of DSE.

Results and discussion

Microstructural and valence state examination

The schematic illustration of the formation of the CNF-LDH-E is provided in Fig. 1. The CNF-LDH was grown through a one-step hydrothermal process (see Methods in ESI†). Next, the stacked layers in the CNF-LDH were exfoliated *via* a facile O_2 plasma treatment, exposing more active sites on the basal plane of the layered structure. The phase of the catalysts was investigated using the powder X-ray diffraction (PXRD) pattern. We investigated the impact of the Ce doping, which was followed by exfoliation, on the phase of the NF-LDH structure (Fig. 2a).

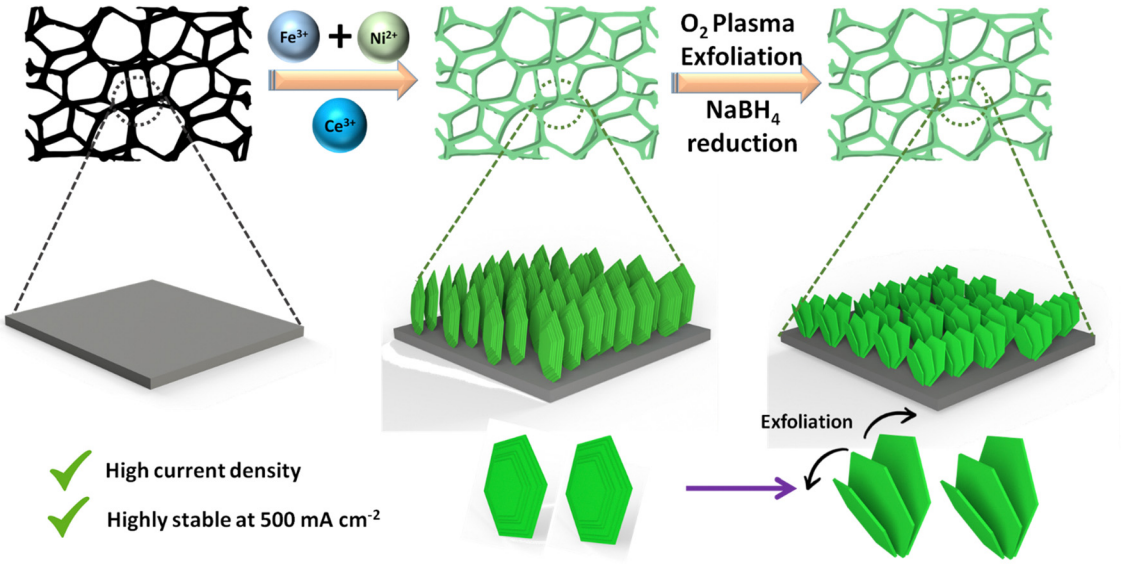

Fig. 1 (a) Schematic of the formation of the CNF-LDH-E.

 © 2025 The Author(s). Published by the Royal Society of Chemistry

Open Access Article. Published on 27 febbraio 2025. Downloaded on 26/12/2025 23:20:05.
This article is licensed under a Creative Commons Attribution-NonCommercial 3.0 Unported Licence.

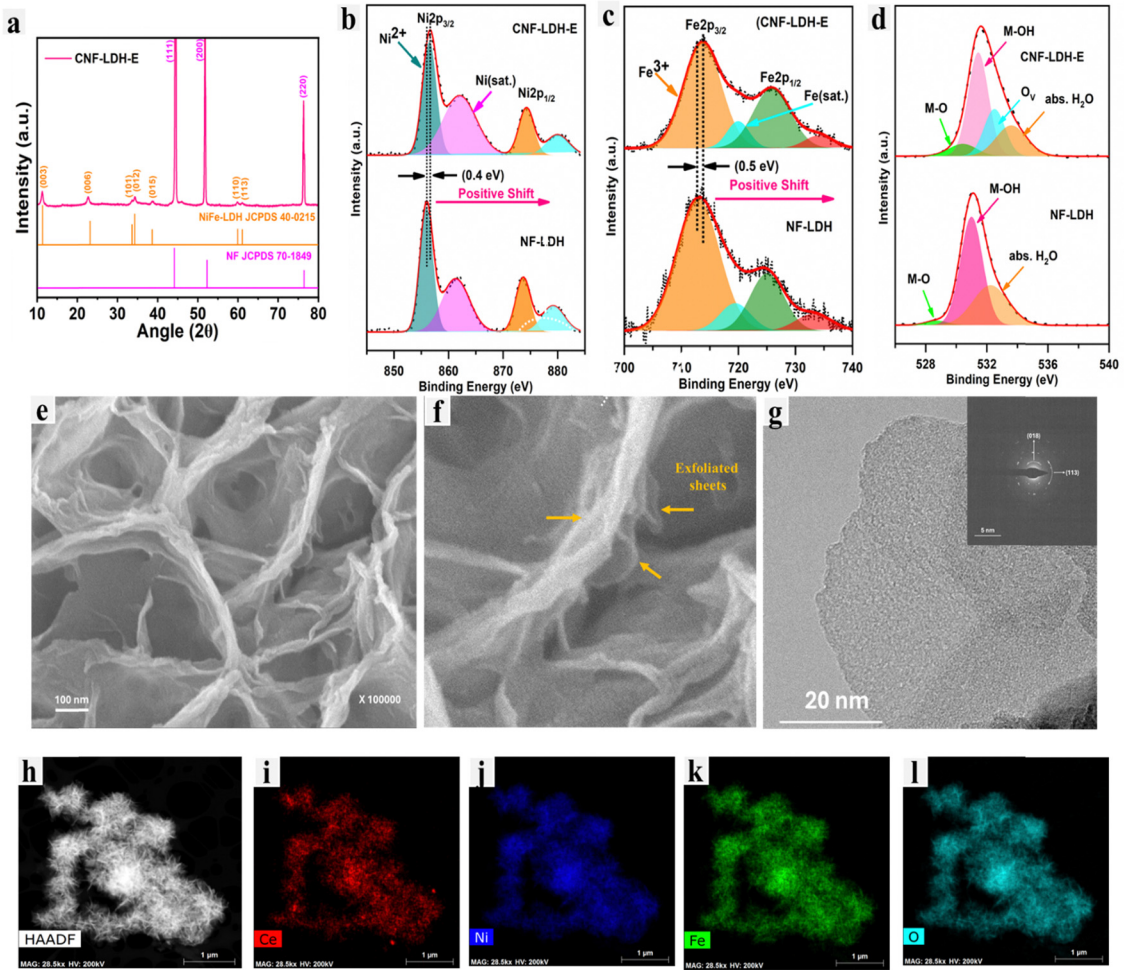

Fig. 2 (a) PXRD pattern of the CNF-LDH-E (b) XPS spectra of Ni 2p (c) Fe 2p and (d) O 1s present in CNF-LDH-E. (e) and (f) SEM images of the exfoliated CNF-LDH-E. (g) TEM image of the CNF-LDH-E (inset-SAED pattern for CNF-LDH-E). (h) STEM-EDS mapping of CNF-LDH-E for confirming the presence of (i) Ce, (j) Ni, (k) Fe and (l) O.

In the NF-LDH structure, the peaks at 11.4°, 22.8°, 34.3°, 39.0°, 46.2°, 59.9° and 61.1° correspond to the (003), (006), (012), (015), (018), (110) and (113) crystal planes (JCPDS 40-0215).[39] The crystal structure of the NF-LDH remains intact after the Ce doping and exfoliation. The valence state change in Ni, Fe and O after the integration of Ce onto the NF-LDH lattice was investigated using X-ray photoelectron spectroscopy (XPS). XPS survey spectra of CNF-LDH-E and NF-LDH are provided in Fig. S1 (ESI†). The high-resolution XPS spectra of Ni 2p for NF-LDH and CNF-LDH are depicted in Fig. 2b. For NF-LDH, the peaks centered at 855.9 eV and 861.3 eV correspond to Ni^{2+} and a satellite peak of Ni $2p_{3/2}$ splitting. Similarly, two peaks were observed for the Ni $2p_{1/2}$ splitting.[40,41] These peaks were also observed in the Ni 2p spectra of CNF-LDH-E at 856.4 and 861.9 eV for Ni^{2+} and a satellite peak of Ni $2p_{3/2}$ splitting. The binding energy for the Ni 2p spectra increases after incorporating Ce, confirming the modulation of the electronic structure of Ni in the form of an increased valence state. The enhancement in the valence state was consistent with the Fe 2p spectra. In the Fe 2p XPS spectra of NF-LDH, the peaks positioned at 713.2 and 713.7 eV correspond to Fe^{3+} and one shake-up peak for the Fe $2p_{3/2}$ splitting (Fig. 2c).[42] The same peaks were observed at 713.7 eV and 714.2 eV for the CNF-LDH. Considering the aforementioned finding, it can be concluded that the integration of Ce into the lattice led to an increase in the valence states of Ni^{2+} and Fe^{3+}. This, in turn, caused a partial shift in the oxidation state, and the new oxidation states for these metals are higher than those of the 2+ and 3+ states. Their characteristics are being driven to produce a harder Lewis acid as a result of the higher oxidation number, which ultimately results in a rise in the capture of the hard Lewis base OH^- selectively over the soft Lewis base Cl^-. Furthermore, the O 1s spectra of NF-LDH depict three peaks centered at 528.7 eV, 530.9 eV, and 532.2 eV, corresponding to the M–O bond, M–OH bond, and adsorbed water molecules on the lattice.[43,44]

Upon comparing the O 1s spectra of NF-LDH and CNF-LDH-E (Fig. 2d), it was seen that the CNF-LDH-E had oxygen vacancies. The XPS spectrum of Ce 3d in CNF-LDH-E is shown in Fig. S2 (ESI†). These vacancies were a result of the $NaBH_4$ treatment of the CNN-LDH during the exfoliation process. The morphological analysis was conducted using transmission and

Open Access Article. Published on 27 febbraio 2025. Downloaded on 26/12/2025 23:20:05.
This article is licensed under a Creative Commons Attribution-NonCommercial 3.0 Unported Licence.

scanning electron microscopy (TEM/SEM). The fine exfoliated sheets of the CNF-LDH-E are shown in Fig. 2e and f. The 2D sheet of the CNF-LDH can also be observed in the TEM images (Fig. 2g). The inset of Fig. 2g depicts the selected area electron diffraction pattern (SAED) of the CNF-LDH-E with the (018) and (113) planes.[43] Furthermore, the STEM energy dispersive X-ray spectroscopy (EDS) mapping was employed for the estimation of the surface uniformity of the elements. The STEM-EDS mapping confirms the fine distribution of Ce, Ni, Fe, and O over the CNF-LDH-E sheet (Fig. 2h and i). The atomic percentage of the elements in the CNF-LDH-E catalyst has been quantified using energy-dispersive X-ray spectroscopy (Fig. S3, ESI†). The obtained atomic percentages of Ce, Fe, Ni and O are 1.23, 6.31, 28.50 and 63.96%, respectively.

X-ray absorption near edge structure (XANES) is highly valuable in resolving the electronic structure of the NF-LDH and CNF-LDH samples. Fig. 3a shows XANES spectra of NF-LDH, CNF-LDH-E, and the Fe_2O_3 standard material at the Fe K-edge. It can be observed that the main edge of the XANES spectra of both NF-LDH and CNF-LDH-E almost overlap with the standard Fe_2O_3 spectrum, indicating the 3+ oxidation state of Fe. However, the position of the main edge in the XANES spectra of Ni K-edge (Fig. 3b) is observed in the middle of the Ni metal and NiO, indicating mixed Ni oxidation states in NF-LDH and CNF-LDH-E samples. However, the pre-edge photon energy of the Ni-K edge and Fe-K edge of the CNF-LDH-E is higher than that of the NF-LDH, indicating the increased valence states of Fe and Ni. This information is in line with the information obtained from the XPS analysis. The XANES spectra at the Ce L3 edge, shown in Fig. S4 (ESI†), of the CNF-LDH and the CeO_2 powder samples show a different peak behaviour. The CNF-LDH-E shows a single main edge peak at a lower energy position, while the CeO_2 powder sample shows a double edge peak with a higher energy position, indicating a significant difference in the local structure. The local structure was further probed using a continuous Cauchy wavelet transform (CCWT), which provides significant information in three dimensions. The CCWT of NF-LDH at Fe K-edge (Fig. 3c) shows the 1st dense peak around 1.64 Å, which corresponds to the Fe–O coordination. The 2nd dense peak was observed around 1.77 Å, which corresponds to the Fe–M (M = metal) coordination. The CCWT of CNF-LDH-E at Fe K-edge (Fig. 3d) shows the 1st dense peak centered at 1.61 Å with more distribution, indicating slight contraction of the Fe–O bond, and the 2nd dense peak was observed centered at 3.48 Å. In the case of Ni K-edge, the CCWT of NF-LDH (Fig. 3e) shows the 1st dense peak around 2.15 Å (Ni–O/M coordination), while the same coordination was noticed at 2.22 Å for CNF-LDH-E (Fig. 3f). Hence, Ni coordination is noted to be different compared to Fe in the samples. Similarly, the CCWT of CNF-LDH-E at Ce L3-edge is noticed differently and the intense peaks are noted at 2.15 Å compared to 1.82 Å of the CeO_2 powder (Fig. S5, ESI†). The EXAFS spectra of the Fe-K edge, Ni-K edge, and Ce-L3 edge are provided in Fig. S6 (ESI†). The CCWT plots of the standards, Ni-foil, NiO, Fe-foil, and Fe_2O_3 are also provided in Fig. S7 (ESI†).

HER and OER properties in alkaline freshwater and seawater

The bifunctional behaviour of the self-standing catalytic electrode towards HER and OER is investigated using the

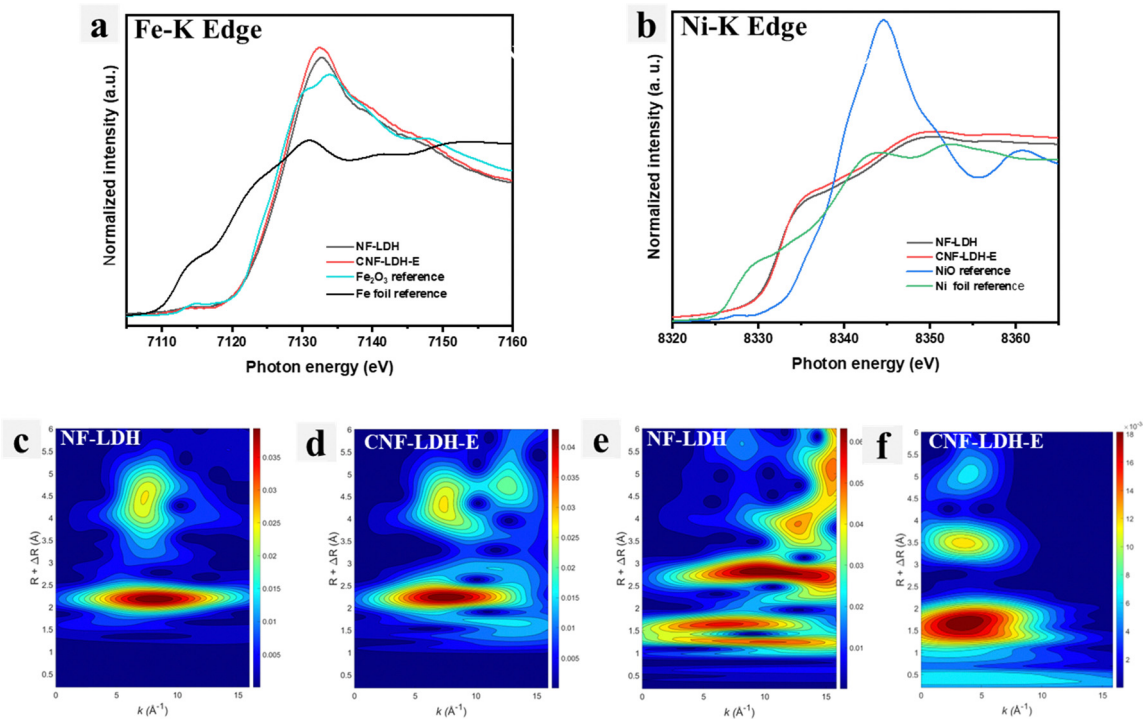

Fig. 3 X-ray absorption near edge (XANES) spectra of (a) Fe-K edge and (b) Ni-K edge, continuous Cauchy wavelet transform (CCWT) plots of Fe-K edge for (c) NF-LDH (d) CNF-LDH-E, and Ni-K edge for (e) NF-LDH and (f) CNF-LDH-E.

 © 2025 The Author(s). Published by the Royal Society of Chemistry

Open Access Article. Published on 27 febbraio 2025. Downloaded on 26/12/2025 23:20:05.
This article is licensed under a Creative Commons Attribution-NonCommercial 3.0 Unported Licence.

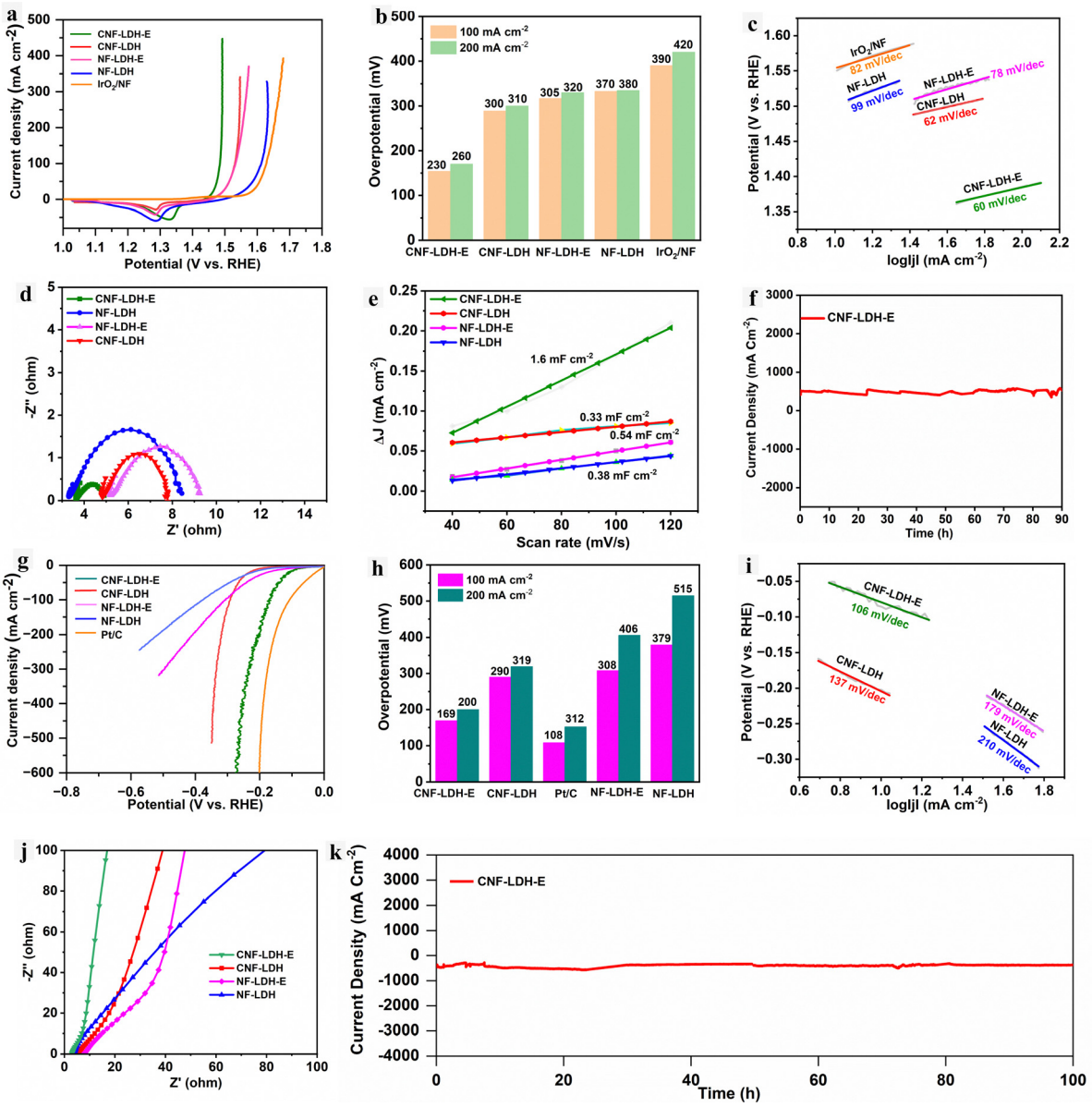

Fig. 4 Electrochemical activity in 1 M KOH solution. (a) Polarization curves for the OER (b) overpotential at the current densities of 100 and 200 mA cm^{-2} for OER (c) Tafel slope of CNF-LDH-E and other control samples for OER (d) EIS Nyquist plot for OER (e) C_{dl} of all the samples (f) durability of the catalyst towards OER (g) polarization curves for the HER (h) overpotential at the current densities of 100 and 200 mA cm^{-2} for OER (i) Tafel plot for HER (j) ESI Nyquist plot for HER (k) durability test at the high current density of 500 mA cm^{-2}.

three-electrode setup. The complete details of the electrochemical procedure and conditions are provided in the Electrochemical section of the ESI.† First, the CNF-LDH-E was tested for the OER, and it exhibits extremely good catalytic activity towards OER with the overpotential of 230 $mV_{\eta100}$, whereas the overpotential obtained for the CNF-LDH, NF-LDH-E, NF-LDH and IrO_2/NF was 300 $mV_{\eta100}$, 305 $mV_{\eta100}$, 370 $mV_{\eta100}$ and 390 $mV_{\eta100}$ (Fig. 4a and b). The overpotential of the catalyst for OER is significantly superior to the recently published state-of-the-art catalyst (Table S1, ESI†). We computed the Tafel slope value from the polarization curves, and the obtained Tafel slope values for the CNF-LDH-E, CNF-LDH, NF-LDH-E, NF-LDH and IrO_2 are 60, 62, 78, 99 and 82 mV dec^{-1} (Fig. 4c). The obtained Tafel slope for the CNF-LDH-E is the lowest among all control samples, suggesting the faster reaction kinetics.[44] The electrode–electrolyte interfacial interaction was investigated by the electrochemical impedance spectroscopy (EIS) analysis (Fig. 4d). When compared with the control samples, the lowest charge transfer resistance was obtained for the CNF-LDH-E sample, which implies that the electron transfer from the interfaces generated between the catalytically active site and the electrolyte is very rapid, resulting in the higher adsorption of the intermediate ion at the electrode surface.[45] Similarly, the electrochemically active surface area (ECSA) was computed with the help of the double-layer capacitance data (C_{dl}). The obtained C_{dl} values for the CNF-LDH-E, CNF-LDH, NF-LDH-E

Open Access Article. Published on 27 febbraio 2025. Downloaded on 26/12/2025 23:20:05. This article is licensed under a Creative Commons Attribution-NonCommercial 3.0 Unported Licence.

and NF-LDH are 1.6, 0.33, 0.54, and 0.38 mF cm^{-2} (Fig. 4e). The higher C_{dl} value for the CNF-LDH-E indicates the existence of a larger number of active sites on the catalyst surface.[46] The LSV curve was further normalized with the ECSA values (Fig. S8, ESI†) and it was found that the intrinsic activity of the catalyst is higher after the ECSA normalization when compared to the other control samples. The cyclic voltammetry curves utilized for the estimation of the C_{dl} are provided in Fig. S9 (ESI†). Durability is the primary determinant of the electrode's resilience under hard environments with high current densities. The durability of the CNF-LDH-E electrode was estimated using the chronoamperometry technique, and the catalyst is highly stable for 90 h by maintaining a higher current density of 500 mA cm^{-2} continuously (Fig. 4f). Under similar conditions, all the samples were also tested for the HER activity. The polarization curves show the overpotential of 169 $mV_{\eta100}$, 290 $mV_{\eta100}$, 108 $mV_{\eta100}$, 308 $mV_{\eta100}$ and 379 $mV_{\eta100}$ for CNF-LDH-E, CNF-LDH, Pt/C, NF-LDH-E and NF-LDH, respectively (Fig. 4g and h). The Tafel slope analysis revealed the lowest Tafel slope of 106 mV dec^{-1} for the CNF-LDH-E and comparatively higher values for the CNF-LDH (137 mV dec^{-1}), NF-LDH-E (179 mV dec^{-1}), NF-LDH (210 mV dec^{-1}) (Fig. 4i). The EIS Nyquist plot confirms the lowest value of the charge transfer resistance for the CNF-LDH-E and comparatively higher values for the control samples (Fig. 4j). The analysis reveals that as for OER the charge transfer through the electrode–electrolyte interface is higher for the CNF-LDH-E catalyst for HER also. The durability of the catalyst was measured using chronoamperometry at a very high current density of 500 mA cm^{-2}. The catalyst maintained the current density for almost 100 h without any significant drop (Fig. 4k). This confirms that the catalyst is highly robust for performing the HER at industrial-scale current densities. The ECSA-normalized LSV curves for the HER are shown in Fig. S10 (ESI†). The intrinsic catalytic activity of the CNF-LDH-E is higher than that of the other control samples.[47,48]

After testing the catalyst in the alkaline freshwater for the bifunctional activity, we tested the activity in the simulated seawater (1 M KOH + 0.5 M NaCl). The obtained overpotential for the OER of CNF-LDH-E is 290 $mV_{\eta100}$, whereas the CNF-LDH, NF-LDH-E, NF-LDH shows the overpotential of 330 $mV_{\eta100}$, 440 $mV_{\eta100}$ and 470 $mV_{\eta100}$ respectively (Fig. 5a). The CNF-LDH-E exhibits the least amount of chloride poisoning, as indicated by the fact that it has the lowest overpotential of the catalyst among all of the control samples. Further, the Tafel slope was computed and the lowest value of 61 mV dec^{-1} was obtained for the CNF-LDH-E when compared to the CNF-LDH (142 mV dec^{-1}), NF-LDH-E (174 mV dec^{-1}), and NF-LDH (189 mV dec^{-1}) (Fig. 5b). Further, EIS was employed for the elucidation of the charge transfer resistance and the lowest value of the R_{ct} was obtained for the CNF-LDH-E, indicating the fast electron transfer (Fig. 5c). The CNF-LDH-E also exhibits good catalytic activity towards HER in the seawater. The obtained overpotential was 285 $mV_{\eta100}$, whereas for CNF-LDH, NF-LDH-E, NF-LDH the corresponding values were 309 $mV_{\eta100}$, 359 $mV_{\eta100}$, 420 $mV_{\eta100}$. The commercially available Pt/C exhibits the overpotential of 145 $mV_{\eta100}$ (Fig. 5d). The Tafel slope for CNF-LDH-E was 96 mV dec^{-1}, which was the lowest when compared to the CNF-LDH (157 mV dec^{-1}), NF-LDH-E (229 mV dec^{-1}) and NF-LDH (279 mV dec^{-1}) (Fig. 5e). Similarly, the charge transfer resistance was also low for the CNF-LDH-E when compared to the other control samples (Fig. 5f). The durability of the catalyst towards HER and OER was tested using chronoamperometry. For both reactions, the catalyst was able to maintain the current density of 100 mA cm^{-2} for 100 h (Fig. 5g and h). The excess amount of the Cl^- in the seawater caused chloride corrosion and formed the oxidized chloride species on the anode. We used the iodide titration method to identify the oxidised chloride species in the electrolyte after the prolonged durability test. The information is provided in Fig. S11 (ESI†), and no colour change was observed after the iodide titration, confirming the excellent chloride resistance properties of the CNF-LDH-E electrode towards seawater oxidation. We have assessed the corrosion behaviour of CNF-LDH-E, CNF-LDH, NF-LDH-E and NF-LDH by the Tafel scans in the simulated seawater electrolyte. All the electrodes were exposed to the electrolyte for a long duration, and the Tafel scan was obtained from the polarization curve taken in the range of −0.15 to 0.2 V (V *vs.* RHE) at the scan rate of 5 mV s^{-1}. The information regarding the corrosion resistance (E_{corr}) and the corrosion current (I_{corr}) was obtained from the Tafel plots (Fig. S12, ESI†). The CNF-LDH-E exhibited a more positive corrosion potential, and the lowest corrosion current compared to CNF-LDH, NF-LDH-E, and NF-LDH, indicating superior corrosion resistance of the electrode.

The STEM-EDS mapping was carried out after the durability test for HER and OER, and we found the uniform distribution of all the elements even after prolonged stability (Fig. S13 and S14, ESI†). The PXRD pattern after the durability test also refers to the excellent stability of the catalyst after long-term HER and OER tests (Fig. S15 and S16, ESI†). After the excellent performance of the CNF-LDH-E in the alkaline freshwater and simulated seawater, we constructed a cell containing CNF-LDH-E as both the anode and cathode. The obtained cell potential is 1.61 and 1.62 V for the alkaline freshwater and seawater electrolyte (Fig. 5i). The overall efficiency of the electrochemical reaction is determined by calculating the faradaic efficiency (F.E.). In this case, we calculated F.E. by the water displacement method in the 2-electrode setup, in which both the parts were separated by the membrane. We obtained 92% of the F.E. in the 2-electrode overall seawater splitting (Fig. 5j). The durability of the catalyst was also tested in the 2-electrode setup for the seawater electrolysis. The catalyst demonstrates excellent durability by maintaining a high current density of 200 mA cm^{-2} for 95 h (Fig. 5k). We also tested the catalytic performance of the catalyst in the alkaline real seawater in which we noted good stability and durability (Fig. S17, ESI†). The obtained overpotential in the real seawater was 289 mV for the HER and 370 for the OER at the current density of 100 mA cm^{-2}. The catalyst also shows a durability for 50 hours by maintaining the current density of 100 mA cm^{-2} for HER and OER.

Mechanistic analysis using theoretical calculation

DFT calculations were implemented to understand the catalytic reaction mechanisms and identify the active sites. The optimum

 © 2025 The Author(s). Published by the Royal Society of Chemistry

Open Access Article. Published on 27 febbraio 2025. Downloaded on 26/12/2025 23:20:05.
This article is licensed under a Creative Commons Attribution-NonCommercial 3.0 Unported Licence.

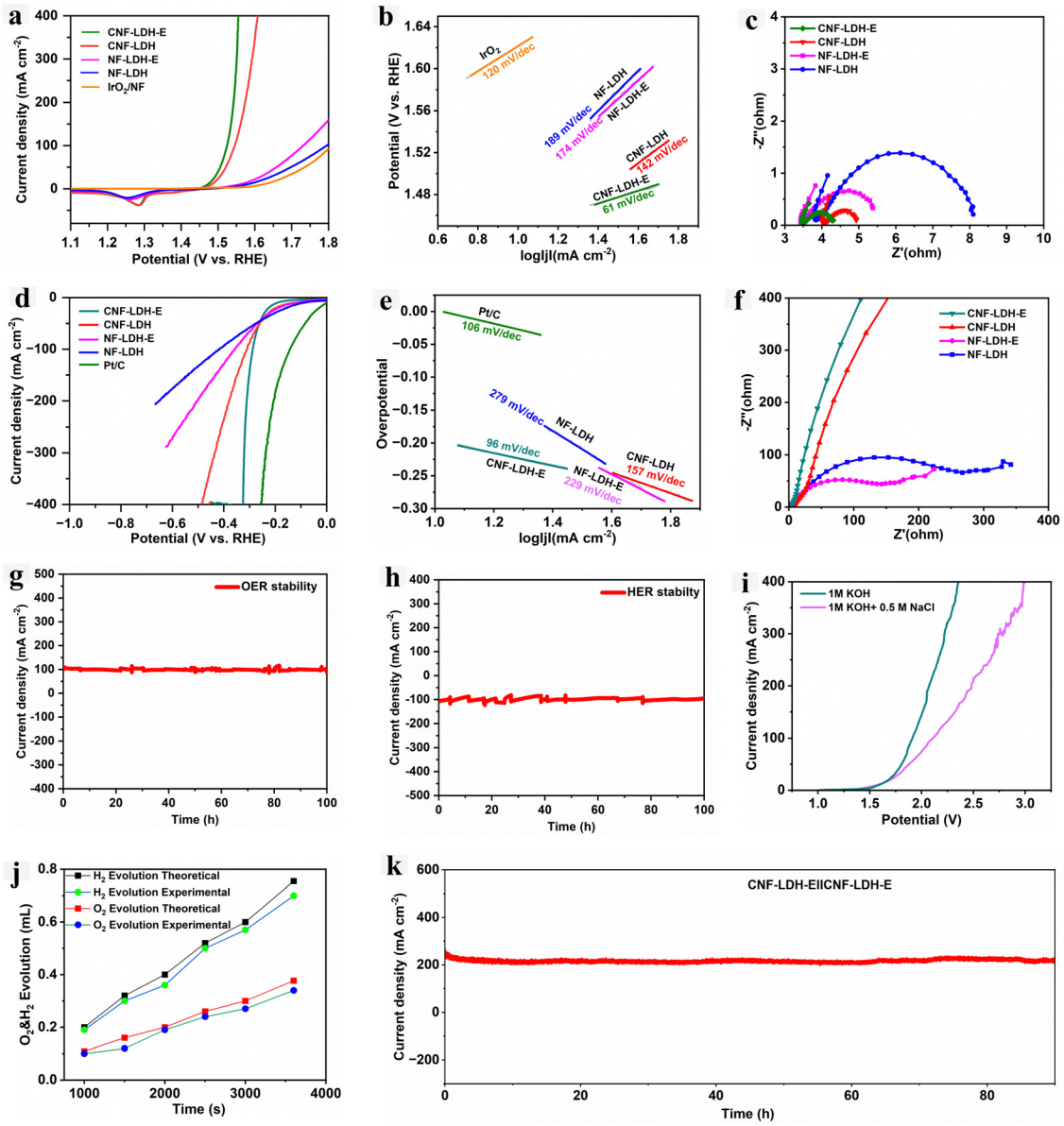

Fig. 5 Electrochemical activity in 1 M KOH + 0.5 M NaCl solution. (a) Polarization curves for the OER. (b) Tafel slope of CNF-LDH-E and other control samples for OER. (c) EIS Nyquist plot for OER. (d) Polarization curves for the HER (e) Tafel plot for HER. (f) ESI Nyquist plot for HER (g) durability test at a high current density of 100 mA cm^{-2} for OER (h) and for HER. (i) Catalytic activity in the 2-electrode cell constructed with CNF-LDH-E as a cathode and anode (j) faradaic efficiency determined using water displacement method. (k) Durability of the catalyst in the 2-electrode setup.

plane for the calculation of the free energy was computed by the estimation of the surface energy for the different planes. The most suitable plane for the DFT calculation was found to be (001) with the lowest surface energies for the intermediate adsorption first, the PDOS plot was computed for the determination of the electron density at the Fermi level for the CNF-LDH-E and it was found that there is a considerable amount of electron density at the Fermi level, which is good for the catalysis (Fig. 6a). Further, we calculated the adsorption energies of Cl* on different sites in the CNF-LDH-E (Fig. 6b and c). Most of the values for the Cl* adsorption on the different catalytic sites are endothermic in nature, suggesting the unfavorable adsorption of the Cl^- onto the catalytic surface. Notably, the Ce–Ni–Ni site exhibited the most favorable adsorption energy for H* (Fig. 6d); for the ideal HER process, the ΔE_{H^*} values should not be more negative or positive. However, it should be close to '0'. These results indicate that the HER active site in the CNF-LDH-E can simultaneously act as an effective chloride-blocking site during seawater splitting. For determining OER reaction pathways, we have analyzed the adsorption of reaction intermediates (*OH, *O and *OOH) on different sites available on the catalyst surface; undoped NF-LDH is also modeled as a control system. The final energy of each intermediate was taken as an average of the different adsorption energies on different hollow positions (*i.e.*, Ce–Ni–Fe, Ce–Ni–Ni, and Ni–Ni–Fe). The potential limiting step (PLS) generally determines the rate-determining step for any multistep reaction.

Open Access Article. Published on 27 febbraio 2025. Downloaded on 26/12/2025 23:20:05.
This article is licensed under a Creative Commons Attribution-NonCommercial 3.0 Unported Licence.

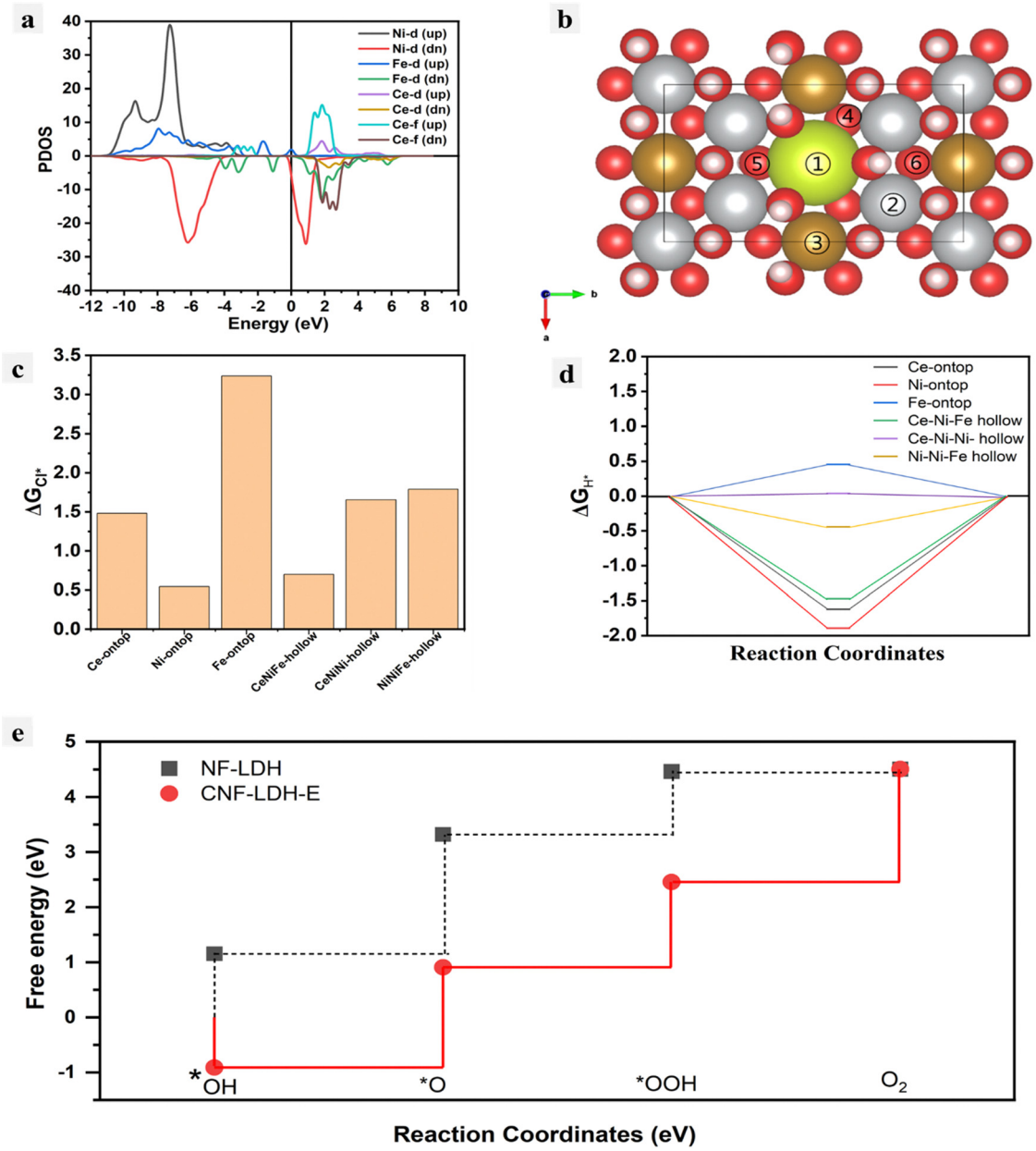

Fig. 6 DFT calculations on the CNF-LDH-E. (a) PDOS plot of the CNF-LDH-E, (b) theoretical model showing the adsorption sites for the adsorption of Cl*, free energy calculation for the (c) Cl* adsorption and (d) H* adsorption and (e) free energy calculations for the different intermediate involved in OER for NF-LDH and NF-LDH-E.

The PLS for the NF-LDH is the transition from *OOH to O_2, whereas the PLS for CNF-LDH-E is the transition from *O to *OOH (Fig. 6d). The lower PLS value for the CNF-LDH-E confirms a better oxygen evolution reaction performance, demonstrating the important role of Ce incorporation into the NF-LDH.

Conclusions

To summarize, the CNF-LDH-E was constructed by the incorporation of Ce into the NF-LDH lattice, followed by the exfoliation step, in which an O_2 plasma treatment was performed. Further, it was found that the electronic structure of NF-LDH was modulated after the Ce incorporation in the form of the enhanced valence state of the Ni^{2+} and Fe^{3+} ions. This enhancement was well investigated by the XPS and XAS studies. Further, the enhanced valence state makes the Ni and Fe centers more Lewis acidic, which enhances the selectivity towards the OH^- capture over Cl^-. The catalyst exhibits excellent catalytic performance towards overall water splitting for alkaline freshwater and alkaline seawater. Further, the experimental findings were verified by the DFT calculations, which

 © 2025 The Author(s). Published by the Royal Society of Chemistry

Open Access Article. Published on 27 febbraio 2025. Downloaded on 26/12/2025 23:20:05.
This article is licensed under a Creative Commons Attribution-NonCommercial 3.0 Unported Licence.

also approve the poor adsorption of Cl^- on CNF-LDH-E. The corrosion resistance was confirmed by the high durability of the CNF-LDH-E electrode in the seawater for almost 100 h. This study proposes a way to adjust the local environment to inhibit chloride ions in saltwater electrolysis. It also presents new opportunities for researchers in the field of seawater electrolysis.

Author contributions

AG and HH conceptualized the idea for this piece of work. AG, JK, JS and EE fabricated the material and completed the characterization part. CC performed the theoretical calculations. AG, JK, HH and TS wrote the manuscript. The final draft of the articles has been reviewed and approved by all the authors.

Data availability

The data supporting this article have been included as part of the ESI.†

Conflicts of interest

There are no conflicts to declare.

Acknowledgements

This research was supported by the Nano & Materials Technology Development Program through the National Research Foundation of Korea (NRF) funded by the Ministry of Science and ICT (RS-2024-00449682). This research was also supported by the Brain Pool program funded by the Ministry of Science and ICT through the National Research Foundation of Korea (Grant No. RS-2023-00284361).

References

1 X. Wang, M. Geng, S. Sun, Q. Xiang, S. Dong, K. Dong, Y. Yao, Y. Wang, Y. Yang, Y. Luo, D. Zheng, Q. Liu, J. Hu, Q. Wu, X. Sun and B. Tang, Recent advances of bifunctional electrocatalysts and electrolyzers for overall seawater splitting, *J. Mater. Chem. A*, 2024, **12**, 634–656.

2 L. Zhang, H. Zhao, S. Xu, Q. Liu, T. Li, Y. Luo, S. Gao, X. Shi, A. M. Asiri and X. Sun, Recent Advances in 1D Electrospun Nanocatalysts for Electrochemical Water Splitting, *Small Struct.*, 2021, **2**, 2000048.

3 A. Midilli, H. Kucuk, M. E. Topal, U. Akbulut and I. Dincer, A comprehensive review on hydrogen production from coal gasification: Challenges and Opportunities, *Int. J. Hydrogen Energy*, 2021, **46**, 25385–25412.

4 P. Sun, B. Young, A. Elgowainy, Z. Lu, M. Wang, B. Morelli and T. Hawkins, Criteria Air Pollutants and Greenhouse Gas Emissions from Hydrogen Production in U.S. Steam Methane Reforming Facilities, *Environ. Sci. Technol.*, 2019, **53**, 7103–7113.

5 R. Carapellucci and L. Giordano, Steam, dry and autothermal methane reforming for hydrogen production: A thermodynamic equilibrium analysis, *J. Power Sources*, 2020, **469**, 228391.

6 Z. Ou, Z. Zhang, C. Qin, H. Xia, T. Deng, J. Niu, J. Ran and C. Wu, Highly active and stable Ni/perovskite catalysts in steam methane reforming for hydrogen production, *Sustainable Energy Fuels*, 2021, **5**, 1845–1856.

7 X. Xiao, L. Yang, W. Sun, Y. Chen, H. Yu, K. Li, B. Jia, L. Zhang and T. Ma, Electrocatalytic Water Splitting: From Harsh and Mild Conditions to Natural Seawater, *Small*, 2022, **18**, 2105830.

8 J. Liu, S. Duan, H. Shi, T. Wang, X. Yang, Y. Huang, G. Wu and Q. Li, Rationally Designing Efficient Electrocatalysts for Direct Seawater Splitting: Challenges, Achievements, and Promises, *Angew. Chem., Int. Ed.*, 2022, **61**, e202210753.

9 L.-W. Shen, Y. Wang, L. Shen, J.-B. Chen, Y. Liu, M.-X. Hu, W.-Y. Zhao, K.-Y. Xiong, S.-M. Wu, Y. Lu, J. Ying, M. M. Titirici, C. Janiak, G. Tian and X.-Y. Yang, Ruthenium nanoparticles decorated with surface hydroxyl and borate species boost overall seawater splitting *via* increased hydrophilicity, *Energy Environ. Sci.*, 2024, **17**, 3888–3897.

10 H. Jin, J. Xu, H. Liu, H. Shen, H. Yu, M. Jaroniec, Y. Zheng and S.-Z. Qiao, Emerging materials and technologies for electrocatalytic seawater splitting, *Sci. Adv.*, 2023, **9**, eadi7755.

11 B. E. Logan, L. Shi and R. Rossi, Enabling the use of seawater for hydrogen gas production in water electrolyzers, *Joule*, 2021, **5**, 760–762.

12 P. Farràs, P. Strasser and A. J. Cowan, Water electrolysis: Direct from the sea or not to be?, *Joule*, 2021, **5**, 1921–1923.

13 S. Dresp, F. Dionigi, M. Klingenhof and P. Strasser, Direct Electrolytic Splitting of Seawater: Opportunities and Challenges, *ACS Energy Lett.*, 2019, **4**, 933–942.

14 H. Fei, R. Liu, T. Liu, M. Ju, J. Lei, Z. Wang, S. Wang, Y. Zhang, W. Chen, Z. Wu, M. Ni and J. Wang, Direct Seawater Electrolysis: From Catalyst Design to Device Applications, *Adv. Mater.*, 2024, **36**, 2309211.

15 H. Chen, J. Yu, L. Liu, R.-T. Gao, Z. Gao, Y. Yang, Z. Chen, S. Zhan, X. Liu, X. Zhang, H. Dong, L. Wu and L. Wang, Modulating Pt–N/O Bonds on Co-doped WO3 for Acid Electrocatalytic Hydrogen Evolution with Over 2000 h Operation, *Adv. Energy Mater.*, 2024, **14**, 2303635.

16 S. Liu, R.-T. Gao, M. Sun, Y. Wang, T. Nakajima, X. Liu, W. Zhang and L. Wang, *In situ* construction of hybrid Co(OH)2 nanowires for promoting long-term water splitting, *Appl. Catal., B*, 2021, **292**, 120063.

17 H. Chen, R.-T. Gao, H. Chen, Y. Yang, L. Wu and L. Wang, Ruthenium And Silver Synergetic Regulation NiFe LDH Boosting Long-Duration Industrial Seawater Electrolysis, *Adv. Funct. Mater.*, 2024, **34**, 2315674.

18 K. Maeda, H. Masuda and K. Domen, Effect of electrolyte addition on activity of $(Ga_{1-x}Zn_x)(N_{1-x}O_x)$ photocatalyst for overall water splitting under visible light, *Catal. Today*, 2009, **147**, 173–178.

Open Access Article. Published on 27 febbraio 2025. Downloaded on 26/12/2025 23:20:05.
This article is licensed under a Creative Commons Attribution-NonCommercial 3.0 Unported Licence.

19 D. R. Kester, I. W. Duedall, D. N. Connors and R. M. Pytkowicz, Preparation of artificial seawater, *Limnol. Oceanogr.*, 1967, **12**, 176–179.
20 M. Cuartero, G. Crespo, T. Cherubini, N. Pankratova, F. Confalonieri, F. Massa, M.-L. Tercier-Waeber, M. Abdou, J. Schäfer and E. Bakker, In Situ Detection of Macronutrients and Chloride in Seawater by Submersible Electrochemical Sensors, *Anal. Chem.*, 2018, **90**, 4702–4710.
21 J. Ren, G. He, X. Deng, X. Deng, Y. Yang, H. Yao and S. Yang, Metallogenesis of Co-rich ferromanganese nodules in the northwestern Pacific: Selective enrichment of metallic elements from seawater, *Ore Geol. Rev.*, 2022, **143**, 104778.
22 S. Jung Kim, H. Choi, J. Ho Ryu, K. Min Kim, S. Mhin, A. Kumar Nayak, J. Bang, M. Je, G. Ali, K. Yoon Chung, K.-H. Na, W.-Y. Choi, S. Yeo, J. Uk Jang and H. Han, Zn-doped nickel iron (oxy)hydroxide nanocubes passivated by polyanions with high catalytic activity and corrosion resistance for seawater oxidation, *J. Energy Chem.*, 2023, **81**, 82–92.
23 H. Liu, X. Zhou, C. Ye, M. Ye and J. Shen, In-situ constructing oxide-anion dual-layer on Ce-B-containing electrode electrolyte interface towards highly corrosive seawater splitting, *Appl. Catal., B*, 2024, **343**, 123560.
24 G. Bahuguna, B. Filanovsky and F. Patolsky, Pioneering practical direct sea water splitting *via* an intrinsically-selective chlorine-phobic nickel polysulphide nanostructured electrocatalyst for pure oxygen evolution, *Nano Energy*, 2023, **111**, 108439.
25 E. Enkhtuvshin, S. Yeo, H. Choi, K. M. Kim, B.-S. An, S. Biswas, Y. Lee, A. K. Nayak, J. U. Jang, K.-H. Na, W.-Y. Choi, G. Ali, K. H. Chae, M. Akbar, K. Y. Chung, K. Yoo, Y.-C. Chung, T. H. Shin, H. Kim, C.-Y. Chung and H. Han, Surface Reconstruction of Ni–Fe Layered Double Hydroxide Inducing Chloride Ion Blocking Materials for Outstanding Overall Seawater Splitting, *Adv. Funct. Mater.*, 2023, **33**, 2214069.
26 H. Qi, K. Huang, F. Pan, R. Ma, C. Lian, H. Liu and J. Hu, Boosting Direct Seawater Electrolysis through Intercalation Engineering of Layered Double Hydroxides, *Ind. Eng. Chem. Res.*, 2023, **62**, 19674–19682.
27 J. Zhu, B. Mao, B. Wang and M. Cao, The dynamic anti-corrosion of self-derived space charge layer enabling long-term stable seawater oxidation, *Appl. Catal., B*, 2024, **344**, 123658.
28 F. Dionigi, T. Reier, Z. Pawolek, M. Gliech and P. Strasser, Design Criteria, Operating Conditions, and Nickel–Iron Hydroxide Catalyst Materials for Selective Seawater Electrolysis, *ChemSusChem*, 2016, **9**, 962–972.
29 X. Jun, H. Jin, T. Lu, J. Li, Y. Liu, K. Davey, Y. Zheng and S.-Z. Qiao, $IrO_x{\cdot}nH_2O$ with lattice water–assisted oxygen exchangefor high-performance proton exchange membranewater electrolyzers, *Sci. Adv.*, 2023, **9**, eadh1718.
30 C. Chen, H. Jin, P. Wang, M. Jaroniec, Y. Zheng and S.-Z. Qiao, Local reaction environment in electrocatalysis, *Chem. Soc. Rev.*, 2024, **53**, 2022–2055.
31 Y. Du, Q. Li, M. Liu, D. Liu, W. Xiao, Z. Xiao, Z. Li, Y. Yamauchi, S. M. Osman, Z. Wu and L. Wang, Cu-based hollow nanotubes with enhanced surface roughness and Chloridion-Enriched environment for Seawater-Splitting, *Chem. Eng. J.*, 2023, **475**, 146057.
32 H. Liu, W. Shen, H. Jin, J. Xu, P. Xi, J. Dong, Y. Zheng and S.-Z. Qiao, High-Performance Alkaline Seawater Electrolysis with Anomalous Chloride Promoted Oxygen Evolution Reaction, *Angew. Chem., Int. Ed.*, 2023, **62**, e202311674.
33 L. Zhuang, J. Li, K. Wang, Z. Li, M. Zhu and Z. Xu, Structural Buffer Engineering on Metal Oxide for Long-Term Stable Seawater Splitting, *Adv. Funct. Mater.*, 2022, **32**, 2201127.
34 J. Guo, Y. Zheng, Z. Hu, C. Zheng, J. Mao, K. Du, M. Jaroniec, S.-Z. Qiao and T. Ling, Direct seawater electrolysis by adjusting the local reaction environment of a catalyst, *Nat. Energy*, 2023, **8**, 264–272.
35 L. Tan, H. Wang, C. Qi, X. Peng, X. Pan, X. Wu, Z. Wang, L. Ye, Q. Xiao, W. Luo, H. Gao, W. Hou, X. Li and T. Zhan, Regulating Pt electronic properties on NiFe layered double hydroxide interface for highly efficient alkaline water splitting, *Appl. Catal., B*, 2024, **342**, 123352.
36 K. Zeng, M. Chao, M. Tian, J. Yan, M. H. Rummeli, P. Strasser and R. Yang, Atomically Dispersed Cerium Sites Immobilized on Vanadium Vacancies of Monolayer Nickel-Vanadium Layered Double Hydroxide: Accelerating Water Splitting Kinetics, *Adv. Funct. Mater.*, 2024, **34**, 2308533.
37 Y. Wang, D. Yan, S. El Hankari, Y. Zou and S. Wang, Recent Progress on Layered Double Hydroxides and Their Derivatives for Electrocatalytic Water Splitting, *Adv. Sci.*, 2018, **5**, 1800064.
38 B. Chen, Z. Zhang, S. Kim, S. Lee, J. Lee, W. Kim and K. Yong, Ostwald Ripening Driven Exfoliation to Ultrathin Layered Double Hydroxides Nanosheets for Enhanced Oxygen Evolution Reaction, *ACS Appl. Mater. Interfaces*, 2018, **10**, 44518–44526.
39 C. Hou, Z. Cui, S. Zhang, W. Yang, H. Gao and X. Luo, Rapid large-scale synthesis of ultrathin NiFe-layered double hydroxide nanosheets with tunable structures as robust oxygen evolution electrocatalysts, *RSC Adv.*, 2021, **11**, 37624–37630.
40 S. Nayak and K. Parida, Superactive NiFe-LDH/graphene nanocomposites as competent catalysts for water splitting reactions, *Inorg. Chem. Front.*, 2020, **7**, 3805–3836.
41 R. Yang, Y. Zhou, Y. Xing, D. Li, D. Jiang, M. Chen, W. Shi and S. Yuan, Synergistic coupling of CoFe-LDH arrays with NiFe-LDH nanosheet for highly efficient overall water splitting in alkaline media, *Appl. Catal., B*, 2019, **253**, 131–139.
42 H. Zhang, X. Li, A. Hähnel, V. Naumann, C. Lin, S. Azimi, S. L. Schweizer, A. W. Maijenburg and R. B. Wehrspohn, Bifunctional Heterostructure Assembly of NiFe LDH Nanosheets on NiCoP Nanowires for Highly Efficient and Stable Overall Water Splitting, *Adv. Funct. Mater.*, 2018, **28**, 1706847.
43 J. Yang and Y. Yang, Boosting the inherent activity of NiFe layered double hydroxide *via* erbium incorporation for water oxidation, *Front. Chem.*, 2023, 11.
44 O. van der Heijden, S. Park, R. E. Vos, J. J. J. Eggebeen and M. T. M. Koper, Tafel Slope Plot as a Tool to Analyze Electrocatalytic Reactions, *ACS Energy Lett.*, 2024, **9**, 1871–1879.
45 H. Sun, W. Zhang, J.-G. Li, Z. Li, X. Ao, K.-H. Xue, K. K. Ostrikov, J. Tang and C. Wang, Rh-engineered ultrathin NiFe-LDH

 © 2025 The Author(s). Published by the Royal Society of Chemistry

Open Access Article. Published on 27 febbraio 2025. Downloaded on 26/12/2025 23:20:05.
This article is licensed under a Creative Commons Attribution-NonCommercial 3.0 Unported Licence.

nanosheets enable highly-efficient overall water splitting and urea electrolysis, *Appl. Catal., B*, 2021, **284**, 119740.

46 X. Wang, J. Wang, J. Liao, L. Wang, M. Li, R. Xu and L. Yang, Surface engineering of superhydrophilic Ni2P@NiFe LDH heterostructure toward efficient water splitting electrocatalysis, *Appl. Surf. Sci.*, 2022, **602**, 154287.

47 N. Attarzadeh, A. Lakshmi-Narayana, D. Das, S. Tan, V. Shutthanandan and C. V. Ramana, One-Step Synthesis and Operando Electrochemical Impedance Spectroscopic Characterization of Heterostructured MoP–Mo2N Electrocatalysts for Stable Hydrogen Evolution Reaction, *ACS Appl. Mater. Interfaces*, 2024, **16**, 6958–6970.

48 Y. Chen, Y. Liu, W. Zhai, H. Liu, T. Sakthivel, S. Guo and Z. Dai, Metastabilizing the Ruthenium Clusters by Interfacial Oxygen Vacancies for Boosted Water Splitting Electrocatalysis, *Adv. Energy Mater.*, 2024, **14**, 2400059.